

April 15, 2018

A new spherically symmetric general relativistic hydrodynamical code.

José V. Romero¹, **José M^a. Ibáñez**²

José M^a. Martí^{2,3}, and **Juan A. Miralles**²

¹ Departamento de Física Teórica

Universidad de Valencia

46100 Burjassot (Valencia), Spain

² Departamento de Astronomía y Astrofísica

Universidad de Valencia

46100 Burjassot (Valencia), Spain

³ Max-Planck-Institut für Astrophysik

Karl-Schwarzschild-str., 1, 8046 Garching bei München, Germany

Abstract

In this paper we present a full general relativistic one-dimensional hydro-code which incorporates a modern high-resolution shock-capturing algorithm, with an approximate Riemann solver, for the correct modelling of formation and propagation of strong shocks. The efficiency of this code in treating strong shocks is demonstrated by some numerical experiments. The interest of this technique in several astrophysical scenarios is discussed.

Key words: Hydrodynamics – Numerical methods – Relativity – Shock waves.

I. INTRODUCTION

Since the pioneering work by May and White (1967) the use of general relativistic and spherically symmetric hydro-codes has been restricted, basically, to the field of stellar collapse and Supernovae. Currently, there are several astrophysical scenarios for which the constraint of spherical symmetry is still a good approximation and where general relativistic hydrodynamical processes are involved: i) Gamma-ray bursters: Models for explaining gamma-ray bursts compatible with the spatial distribution derived from the BATSE experiment from the Compton Observatory are based on relativistic fireballs originating from the sudden release of energy in small regions (Mészáros et al. 1993, Piran et al. 1993). ii) Spherical accretion onto compact objects: Theoretical studies of spectral properties of X-ray radiation produced in atmospheres around an accreting neutron star have particular importance given the observational capabilities of present instrumentation on board satellites. In particular cases – low magnetic fields, for example – the assumption of spherical symmetry is adequate. iii) Stellar collapse: Different topics of current interest in the field of stellar collapse and supernovae are, apart from the theoretical problem of black hole formation (see, e.g., Baumgarte, Shapiro and Teukolsky 1994), the equation of state for dense matter, the role of neutrinos, the influence of convective motions, etc.. One of them is the correct modelling of formation and propagation of the shock formed after bounce, the so-called *prompt phase*. This question remains of crucial importance as an initial mechanism leading, with the help of other processes involved in the different versions of the *delayed mechanism* – neutrino energy deposition (Bethe and Wilson 1985), convective motions (Janka and Müller 1993, Herant et al. 1994) –, to the final success of the explosion.

The presence of strong shocks is a common feature in the above astrophysical scenarios. Shocks are discontinuous solutions of the hydrodynamical equations and are an important source of numerical problems and inaccuracies. The correct modelling of strong shocks is one of the most delicate issues in – both Newtonian and relativistic – hydrodynamical codes.

May and White's code was built up by using standard finite difference techniques and incorporates an artificial viscosity term to damp down spurious numerical oscillations around discontinuities. Up to date, codes based on the original formulation of May and White and on later versions (e.g., Van Riper 1979) have been used in many supernovae calculations (see, e.g., the recent paper by Swesty, Lattimer and Myra 1994 and references cited therein). The Lagrangian character of May and White's code together with other theoretical considerations concerning the particular coordinate gauge, has prevented its extension to multidimensional calculations.

The first Eulerian code to solve the equations of relativistic hydrodynamics comes from the work of Wilson (1972, 1979). The main ideas of Wilson's procedure laid the foundations of several codes developed in the first half of the eighties which have been applied to several astrophysical scenarios: axisymmetric stellar collapse (Piran 1980, Stark and Piran 1987, Nakamura et al. 1980, Nakamura 1981, Nakamura and Sato 1982, Evans 1986), accretion onto compact objects (Hawley et al. 1984, Petrich et al. 1989) and numerical cosmology (Centrella and Wilson 1984). All of these codes make use of a combination

of artificial viscosity and upwind techniques in order to obtain numerical solutions of the relativistic hydrodynamical equations. On the other hand, the equations are written as a set of advection equations, so the terms containing derivatives (in space or time) of the pressure are treated as source terms. This procedure breaks down (numerically) the *conservative* character of the relativistic hydrodynamics system of equations (see below).

Concerning the present work, during the last decade a number of new *shock-capturing* finite difference approximations have been constructed and found to be very useful in the numerical simulation of classical (Newtonian) fluid dynamics (see, e.g., LeVeque 1992). In addition to conservation form, these schemes are usually constructed to have the following properties: a) Stable and sharp discrete shock profiles. b) High accuracy in smooth regions of the flow. Schemes with these characteristics are usually known as *high-resolution shock-capturing* schemes (henceforth HRSC). They avoid the use of artificial viscosity terms when treating discontinuities and, after extensive experimentation, they appear to be a solid alternative to classical methods with artificial viscosity.

Our spherically symmetric general relativistic hydro-code is the cumulative result of our experience in HRSC schemes applied to Newtonian and special-relativistic fluid dynamics (see Ibáñez 1993, for a review). In previous papers (Martí et al. 1991, Marquina et al. 1992) HRSC schemes have been extended to solve the relativistic hydrodynamics system of equations in one spatial dimension. The procedure relied on two main points: 1) To write the equations of relativistic hydrodynamics as a system of *conservation laws* and identify the suitable vector of unknowns. 2) An *approximate Riemann solver* built up from the spectral decomposition of the Jacobian matrix of the system at the boundaries of each numerical cell. Schneider et al. (1993) have also explored the ultrarelativistic regime with a different Riemann solver. The multidimensional extension of our special-relativistic hydro-code can be found in Font et al. (1994). Similar results have been independently derived by Eulderink (1993). Recently, Martí and Müller (1995) have built up a relativistic version of the popular Newtonian Piecewise Parabolic Method (PPM, Colella and Woodward 1984) and have carried out simulations of relativistic jets with Lorentz factors greater than 20 (Martí et al. 1995a).

Finally, note that in recent years, techniques other than the standard finite difference ones have been applied to simulate relativistic flows. Gourgoulhon (1991, 1992) made use of the accuracy of *spectral methods* (Gottlieb and Orszag 1977) to detect the zero value of the fundamental mode against radial oscillations of a neutron star at the maximum of the mass-radius curve for a given equation of state. Although the global error on the solution decreases exponentially with the number of degrees of freedom, the handling of shock waves by spectral methods remains a major problem due to the Gibbs phenomenon. By combining moving grids and shock tracking techniques Bonazzola and Marck (1991) have obtained promising results for one-dimensional flows. A different numerical approach is provided by *smooth particle hydrodynamics* (Gingold and Monaghan 1977, Lucy 1977), the first application to simulate relativistic flows being made by Mann (1991). These results, although encouraging, are still far from those obtained with HRSC methods.

General relativistic hydrodynamics links gravitational field with geometry, hence, from the numerical point of view, new difficulties arise due to the nonlienarities introduced

by the geometrical terms. The system of equations is coupled not only by Lorentz-like factors, as in special relativity (see Norman and Winkler, 1986 for a discussion on the numerical difficulties), but also by the different components of the metric tensor. In the present paper we describe the features of a full general relativistic hydrodynamical code (some preliminary results were presented in Ibáñez et al. 1992) having the following main properties: i) The code makes use of an approximate Riemann solver which allows to capture shocks in a consistent way. It is a natural extension to general relativistic fluid dynamics of modern HRSC schemes. ii) By using splitting techniques the code can be easily extended to the multidimensional case once the behaviour of the characteristic fields is known.

The structure of this work is as follows: Section §II is devoted to display the full equations of general relativity in a spherically symmetric space-time as well as to the theoretical analysis of this system considered as a system of conservation laws. The hydro-code is based on a numerical algorithm which is explained in §III. Some numerical tests and astrophysical applications are shown in §IV. Finally, a summary of our main conclusions is presented in §V.

II. GENERAL RELATIVISTIC EQUATIONS IN SPHERICAL SYMMETRY AS A SYSTEM OF CONSERVATION LAWS

Let \mathcal{M} be a general spacetime, described by the four dimensional metric tensor $g_{\mu\nu}$. According to the $\{3+1\}$ formalism, the metric is split into the objects α (*lapse*), β^i (*shift*) and γ_{ij} , keeping the line element in the form:

$$ds^2 = -(\alpha^2 - \beta_i \beta^i) dt^2 + 2\beta_i dx^i dt + \gamma_{ij} dx^i dx^j \quad (1)$$

where Greek (Latin) indices run through all (spatial) coordinates.

In the case of spherically symmetric space-times the general relativistic equations can be given in a simple way which looks like the Newtonian hydrodynamics. To this aim the choice of coordinates is crucial. Schwarzschild-type coordinates (Bondi 1964) allow a simple extension of the Eulerian Newtonian hydrodynamics to the Einsteinian one. In terms of slicing of space-time, Schwarzschild-type coordinates are the realization of a *polar time slicing*, a *radial gauge* (see Gourgoulhon 1991), and the generalization of the Schwarzschild coordinates, in terms of which the vacuum and static space-time is described.

The choice of the radial gauge leads to the following expression for the 3-metric

$$\gamma_{ij} = \text{diag}(X^2, r^2, r^2 \sin^2 \theta) \quad . \quad (2)$$

The choice of the polar slicing condition, in spherical symmetry and the radial gauge implies a zero-shift vector ($\beta^i = 0, \forall i$). In the following, we will use the acronym RGP (radial gauge and polar slicing) for the particular spacetime in which we are interested:

$$ds^2 = -\alpha^2 dt^2 + X^2 dr^2 + r^2(d\theta^2 + \sin^2 \theta d\phi^2) \quad . \quad (3)$$

By analogy with the well-known Schwarzschild solution for vacuum, we can define the functions $\Phi(r, t)$ and $m(r, t)$ by

$$X(r, t) = \left(1 - \frac{2m(r, t)}{r}\right)^{-1/2}, \quad \alpha(r, t) = \exp\{\Phi(r, t)\} . \quad (4)$$

The equations describing the evolution of matter are the expression of the *local conservation* of baryon number

$$\nabla_\mu J^\mu = 0 , \quad (5)$$

and the *local conservation* of energy-momentum

$$\nabla_\mu T^{\mu\nu} = 0 , \quad (6)$$

The current J^μ and the energy-momentum tensor $T^{\mu\nu}$ are

$$J^\mu = \rho u^\mu , \quad (7)$$

$$T_{\mu\nu} = \rho h u_\mu u_\nu + p g_{\mu\nu} , \quad (8)$$

where ∇_μ is the covariant derivative, u^μ the four-velocity of the fluid, ρ the rest-mass density, p the pressure, and h the specific enthalpy defined by $h = 1 + \varepsilon + p/\rho$, where ε is the specific internal energy.

The expression chosen for the energy-momentum tensor is that of a perfect fluid and we therefore ignore effects due to heat conduction or viscous interactions.

Let us introduce the *physical velocity*, v , defined by $v = Xu^r/\alpha u^t$. This quantity represents the fluid velocity relative to an observer at rest in the coordinate frame. The Lorentz-like factor $W = \alpha u^t$, satisfies the familiar relation with v , $W = (1 - v^2)^{-1/2}$.

With the above coordinate conditions and the following set of unknown variables

$$\begin{aligned} D &= \alpha X J^t = X \rho W , \\ S &= \alpha T^{tr} = \rho h W^2 v , \\ \tau &= \alpha^2 T^{tt} - D = \rho h W^2 - p - D , \end{aligned} \quad (9)$$

the general relativistic equations can be written as a system of conservation laws (with sources):

$$\frac{\partial \mathbf{u}}{\partial t} + \frac{1}{r^2} \frac{\partial}{\partial r} \left(\frac{r^2 \alpha}{X} \mathbf{f}(\mathbf{u}) \right) = \mathbf{s}(\mathbf{u}) , \quad (10)$$

where

$$\mathbf{u} = (D, S, \tau) , \quad (11)$$

is the *vector of unknowns* which define the state of the system. The *fluxes*, \mathbf{f} , are defined as

$$\mathbf{f} = (Dv, Sv + p, S - Dv) , \quad (12)$$

and the *source terms* (free of derivatives of hydrodynamic quantities) are

$$\mathbf{s}(\mathbf{u}) = \left(0, (Sv - \tau - D)(8\alpha X \pi r p + \alpha X \frac{m}{r^2}) + \alpha X p \frac{m}{r^2} + \frac{2\alpha p}{X r}, 0 \right) . \quad (13)$$

The above system of equations is closed by an equation of state (EOS), that we will assume of the form

$$p = p(\rho, \epsilon) , \quad (14)$$

and the Einstein equations which furnish conditions on the quantities $m(r, t)$ and $\Phi(r, t)$ (see, Gourgoulhon 1991):

$$\frac{\partial m}{\partial r} = 4\pi r^2(\tau + D) , \quad (15)$$

$$\frac{\partial \Phi}{\partial r} = X^2 \left(\frac{m}{r^2} + 4\pi r(p + Sv) \right) , \quad (16)$$

Indeed, by analogy with the static case, we can distinguish (for a given spherical surface having an area $4\pi r^2$) between the enclosed *gravitational mass* m defined by (15) and the enclosed *baryonic mass* m_A defined by

$$\frac{\partial m_A}{\partial r} = 4\pi r^2 D . \quad (17)$$

Equations (15) and (17) are integrated, at each time step, between $r = 0$ and $r = R(t)$ (the radius of the star) with the following boundary conditions: $m(r = 0) = 0$, $m_A(r = 0) = 0$, $m(R(t)) = M$ (the total gravitational mass), $m_A(R(t)) = M_A$ (the total baryonic mass). The gravitational potential Φ , given by equation (16), is defined with the exception of an additive arbitrary constant and is matched at the surface with the exterior Schwarzschild's solution, i.e., $\Phi(R(t)) = (1/2)\ln(1 - 2M/R(t))$. The integration of Φ starts with a zero value at the center and by comparing, at the surface, the integrated value of Φ with the matching condition it is possible to obtain the arbitrary additive constant.

It is worth pointing out that the system of equations (10) displays a very important feature, that is, the conservation of baryonic mass and energy. In effect, the first and third equations of system (10) lead (when acting on integral quantities) to the following relations:

$$\begin{aligned} \frac{\partial M_A}{\partial t} &= -\frac{\alpha}{X} D v \Big|_{R(t)} , \\ \frac{\partial E_b}{\partial t} &= -\frac{\alpha}{X} (S - D) v \Big|_{R(t)} . \end{aligned} \quad (18)$$

The quantity $E_b = M - M_A$, on the analogy of the static case, can be considered as the binding energy of the star. The symbol $|_{R(t)}$ means that the quantities on the right hand side of these equations are evaluated at the surface. Hence, if the boundary conditions at

the surface are zero (i.e., $\rho = \epsilon = 0$, or $v = 0$), the conservation of M_A and E_b (or M) is strictly satisfied.

A numerical algorithm written in conservation form, like the one used in the present paper (see below), preserves numerically this important property of the system. Hence, the correct choice of the vector of unknowns \mathbf{u} , and consequently, source terms $\mathbf{s}(\mathbf{u})$ is of crucial importance.

From the *conserved* quantities $\mathcal{C} = \{D, S, \tau\}$ we must obtain the set of *primitive variables* $\varphi = \{\rho, v, \epsilon\}$, at each time step, by solving an implicit equation in pressure. A one-dimensional Newton-Raphson routine suffices to obtain φ (see Martí & Müller 1995, for details). In the Newtonian limit, the set of new variables $\mathcal{C} = \{D, S, \tau\}$ tends to the set $\{\rho, \rho v, e\}$, with $e = \rho\epsilon + (1/2)\rho v^2 - m/r$, i.e., the density, momentum density and total energy density, respectively.

The hyperbolic character of the relativistic hydrodynamic system of equations has been the subject of study of many authors (see Anile, 1989 and references therein).

As we will show in the next section, Godunov-type methods, or modern HRSC schemes, incorporate the resolution of *local Riemann problems*, initial value problems for system (10) with discontinuous data. In order to extend HRSC to our problem is crucial to know the spectral decomposition of the Jacobian matrix $\mathcal{B}(\mathbf{u})$ of the system (10):

$$\mathcal{B} = \frac{\partial \mathbf{f}(\mathbf{u})}{\partial \mathbf{u}} . \quad (19)$$

Following a procedure similar to the one described in Font et al. (1994), we have derived the eigenvalues and right-eigenvectors of $\mathcal{B}(\mathbf{u})$.

The *eigenvalues*, the characteristic speeds associated with *material waves* and *acoustic waves*, are respectively,

$$\lambda_0 = v , \quad (20)$$

and

$$\lambda_{\pm} = \frac{v \pm c_s}{1 \pm vc_s} , \quad (21)$$

where c_s is the *local sound velocity* which satisfies

$$hc_s^2 = \chi + (p/\rho^2)\kappa , \quad (22)$$

with $\chi = (\partial p/\partial \rho)_{\epsilon}$ and $\kappa = (\partial p/\partial \epsilon)_{\rho}$.

These eigenvalues are the natural extension to our generic space-time of the corresponding characteristic speeds well-known in Minkowski space-time or in Newtonian fluid dynamics. Let us point out that they seem like in Minkowski space-time due to our definitions of velocity and flux.

The *right-eigenvectors* are:

$$\mathbf{r}_0 = \left(\frac{X\tilde{\kappa}}{hW(\tilde{\kappa} - c_s^2)}, v, 1 - r_0^{(1)} \right) , \quad (23)$$

$$\mathbf{r}_{\pm} = \left(\frac{X(1 - \lambda_{\pm}v)}{hW(1 - v^2)}, \lambda_{\pm}, 1 - r_{\pm}^{(1)} \right) , \quad (24)$$

where $\tilde{\kappa} = \kappa/\rho$, and $r_{0,\pm}^{(1)}$ is the first component of the corresponding eigenvector.

The above system (10) is strictly hyperbolic since the Jacobian matrix $\mathcal{B}(\mathbf{u})$ has real and distinct eigenvalues.

III. OUR MODERN HIGH-RESOLUTION SHOCK-CAPTURING SCHEME

In order to exploit numerically the conservative character of the system (10) we have written it as a hyperbolic system of conservation laws (see Lax 1972, for a mathematical analysis). Let us summarize in this Section the main features of our algorithm (see also Martí et al. 1991).

At each time level, the data are the *cell averages* of the conserved quantities

$$\bar{\mathbf{u}}_j^n = \frac{1}{r_j^2 \Delta r_j} \int_{r_{j-\frac{1}{2}}}^{r_{j+\frac{1}{2}}} \mathbf{u}(r, t^n) r^2 dr . \quad (25)$$

The data are advanced in time according to a version of the *method of lines*:

$$\frac{d\bar{\mathbf{u}}_j(t)}{dt} = -\frac{A_{j+\frac{1}{2}} \hat{\mathbf{f}}_{j+\frac{1}{2}} - A_{j-\frac{1}{2}} \hat{\mathbf{f}}_{j-\frac{1}{2}}}{r_j^2 \Delta r_j} + \bar{\mathbf{s}}_j , \quad (26)$$

where

$$\hat{\mathbf{f}}_{j+\frac{1}{2}} = \hat{\mathbf{f}}(\mathbf{u}_{j-1}, \mathbf{u}_j, \mathbf{u}_{j+1}) , \quad (27)$$

is a consistent *numerical flux* vector, i.e., $\hat{\mathbf{f}}(\mathbf{u}, \mathbf{u}, \mathbf{u}) = \mathbf{f}(\mathbf{u})$. The quantity $A_{j+\frac{1}{2}}$ is a combination of the geometrical factors

$$A_{j+\frac{1}{2}} = \left(\frac{r^2 \alpha}{X} \right)_{j+\frac{1}{2}} , \quad (28)$$

evaluated at the interface $j + \frac{1}{2}$, and $\bar{\mathbf{s}}_j$ is the cell average of the source terms calculated according to (25).

Once the procedure to evaluate $\hat{\mathbf{f}}_{j+\frac{1}{2}}$ is known, then system (26) can be integrated in time by using a suitable ordinary differential equation solver. We have made use of a standard predictor-corrector method. The value of the timestep is constrained by the Courant condition.

A *reconstruction procedure* of the solution at the time level t^n from its cell averages allows us to define local Riemann problems at each interface $j + \frac{1}{2}$. We have used a monotonicity preserving linear reconstruction of the primitive variables using the *minmod* function as a 'slope limiter' (Van Leer, 1979). Accordingly, the corresponding values of $\mathbf{u}_{j+\frac{1}{2}}$ at the interface $j + \frac{1}{2}$ are:

$$\mathbf{u}_{j+\frac{1}{2}}^L = \bar{\mathbf{u}}_j^n + \mathbf{S}_j^n (r_{j+\frac{1}{2}} - r_j) , \quad (29)$$

$$\mathbf{u}_{j+\frac{1}{2}}^R = \bar{\mathbf{u}}_{j+1}^n + \mathbf{S}_j^n(r_{j+\frac{1}{2}} - r_{j+1}) \quad , \quad (30)$$

where \mathbf{S}_j^n is a *slope limiter* defined by

$$\mathbf{S}_j^n = \text{minmod} \left(\frac{\bar{\mathbf{u}}_{j+1}^n - \bar{\mathbf{u}}_j^n}{r_{j+1} - r_j}, \frac{\bar{\mathbf{u}}_j^n - \bar{\mathbf{u}}_{j-1}^n}{r_j - r_{j-1}} \right) \quad , \quad (31)$$

and the *minmod* function makes a choice of the slope which is minimum or takes a zero when they have different signs:

$$\text{minmod}(a, b) = \begin{cases} a & \text{if } |a| < |b|, ab > 0 \\ b & \text{if } |a| > |b|, ab > 0 \\ 0 & \text{if } ab \leq 0 \end{cases} .$$

At each cell interface the i^{th} component of the *numerical flux* is computed as follows

$$\hat{f}_{j+\frac{1}{2}}^{(i)} = \frac{1}{2} \left(f^{(i)}(\mathbf{u}_{j+\frac{1}{2}}^L) + f^{(i)}(\mathbf{u}_{j+\frac{1}{2}}^R) - \sum_{\alpha=0,\pm} |\tilde{\lambda}_\alpha| \Delta \tilde{\omega}_\alpha \tilde{r}_\alpha^{(i)} \right) \quad , \quad (32)$$

where L and R stand for the left and right states at a given interface $j + \frac{1}{2}$, $\tilde{\lambda}_\alpha$ and $\tilde{r}_\alpha^{(i)}$ ($\alpha = 0, \pm$) are respectively, the eigenvalues and the i^{th} -component of the α -right eigenvector of the Jacobian matrix

$$\mathcal{B}_{j+\frac{1}{2}} = \left(\frac{\partial \mathbf{f}(\mathbf{u})}{\partial \mathbf{u}} \right)_{\mathbf{u}=\frac{1}{2}(\mathbf{u}_{j+\frac{1}{2}}^R + \mathbf{u}_{j+\frac{1}{2}}^L)} . \quad (33)$$

The quantities $\Delta \tilde{\omega}_\alpha$, the jumps in the local characteristic variables across each cell interface, are obtained from

$$\mathbf{u}_{j+\frac{1}{2}}^R - \mathbf{u}_{j+\frac{1}{2}}^L = \sum_{\alpha=0,\pm} \Delta \tilde{\omega}_\alpha \tilde{\mathbf{r}}_\alpha . \quad (34)$$

$\tilde{\lambda}_\alpha$, $\tilde{\mathbf{r}}_\alpha$ and $\Delta \tilde{\omega}_\alpha$, as functions of \mathbf{u} , are evaluated at each interface and, therefore, they depend on the particular values $\mathbf{u}_{j+\frac{1}{2}}^L$ and $\mathbf{u}_{j+\frac{1}{2}}^R$.

With the above ingredients, our algorithm is conservative, upwind, and due to the particular cell-reconstruction, monotone. It is globally second order accurate, although this statement is only well-founded for scalar equations, equally spaced grids, and the smooth part of the flow.

Finally, let us comment on one of the features of our code, its *modularity*. It has been constructed to allow for easy substitution of different Riemann solvers and different cell reconstructions. It also works in Newtonian and special relativistic hydrodynamics.

IV. NUMERICAL EXPERIMENTS AND ASTROPHYSICAL APPLICATIONS

Modern numerical codes must be, and in fact are, checked against well-known analytical solutions before their exploitation in applications. A long battery of test-beds addressed to check hydrodynamical codes exists. The most popular ones are the *standard shock problems* in different symmetries, planar (shock-tube tests), cylindrical or spherical. Their corresponding analytical solutions (in Newtonian fluid dynamics) can be found in standard textbooks (see, e.g., Courant and Friedrichs 1948). The one-dimensional solution of the Riemann problem for relativistic hydrodynamics has been derived recently by Martí and Müller (1994) allowing for the analytical solution of any initial value problem. In previous papers we have carried out numerical experiments in *planar symmetry* with the following standard shock-tube problems: Sod's test, blast wave and shock reflection tests, in both Newtonian and special-relativistic hydrodynamics (see Martí et al. 1991, and Marquina et al. 1992). Here, in Section §IV.1, we have concentrated on the *relativistic spherical shock reflection* problem, which allows to check special relativistic dynamics in a spherically symmetric geometry.

A second test (see Section §IV.2) is the *spherical accretion* onto a self-gravitating object, including general relativistic effects. This test has the advantage of allowing one to check stationary solutions of general relativistic hydrodynamics on a fixed background.

A third test (see Section §IV.3) underwent by our hydro-code is the detection of the *zeros of the fundamental mode* against radial oscillations of a spherical equilibrium configuration, which checks the stability of equilibrium solutions.

In Section §IV.4, we have analyzed Oppenheimer-Snyder collapse. This is one of the standard tests for spherically symmetric, fully relativistic codes, which allows one to check general relativistic dynamics.

With the above selection of tests we span a broad range of different features: special relativistic effects, geometrical effects, general relativistic effects in a background and fully general relativistic dynamics.

Finally, in Section §IV.5 we have carried out an analysis of the dynamics of the general relativistic collapse of compact objects.

IV.1 Relativistic spherical shock reflection

Noh (1987) has exhaustively analyzed the *spherical shock reflection* problem in the Newtonian dynamics of ideal gases ($p = (\Gamma - 1)\rho\varepsilon$). Noh's paper is, in fact, devoted to the study of intrinsic errors which appear when using artificial viscosity techniques in spherically symmetric applications. We have considered the relativistic version of this numerical experiment. The relativistic spherical shock reflection is a severe test due to the difficulties connected with the geometry and, in its relativistic version, with strong nonlinearities induced by the Lorentz factor in the ultrarelativistic regime.

Analytical solutions for the relativistic shock reflection with planar, cylindrical and spherical symmetry can be found in Martí et al. (1995b). The initial data consists of an inflowing cold (i.e., $\varepsilon = 0$) gas with coordinate velocity v and corresponding Lorentz factor W . In the spherical case, the flow converges towards the center and its reflection causes the compression and heating of the gas as it converts its momentum into internal energy. A shock is formed which starts to propagate through the inflowing gas. Behind

the shock the gas is at rest and, according to the conservation of energy accross the shock, has a specific internal energy given by

$$\varepsilon^+ = W - 1. \quad (35)$$

The jump in density at the shock is defined by $\Delta\rho = \rho^+/\rho^-$, where ρ^+ and ρ^- are the postshock and preshock values, respectively. For a relativistic strong shock, like the one developed herein, this jump satisfies

$$\Delta\rho = \frac{\Gamma W + 1}{\Gamma - 1}, \quad (36)$$

with a shock velocity given by

$$v_s = \frac{(\Gamma - 1)W|v|}{W + 1}. \quad (37)$$

In the nonshocked part of the flow (i.e., $r \in]v_s t, \infty[$), the proper rest-mass density distribution is given by

$$\rho = \left(1 + \frac{vt}{r}\right)^2 \rho_0 \quad (38)$$

where ρ_0 is the rest-mass density at infinity.

It is worthwhile to point out one relevant difference between classical and relativistic shocks. In the relativistic case, the jump in density is unbounded, whereas in the present test, the ultrarelativistic regime leads to the following asymptotic relations ($\rho_0 = 1$),

$$\begin{aligned} \Delta\rho &\rightarrow \frac{\Gamma}{\Gamma - 1} W, \\ \rho^+ &\rightarrow \left(\frac{\Gamma}{\Gamma - 1}\right)^3 W, \\ v_s &\rightarrow (\Gamma - 1). \end{aligned} \quad (39)$$

The initial data for this problem are defined in a unit sphere ($0 \leq r \leq 1$) and for an ideal gas with $\Gamma = 4/3$; $v(r, 0) = -v_0$ ($v_0 > 0$), $\rho(r, 0) = \rho_0 = 1$, $\varepsilon(r, 0) = \varepsilon_0 = 0$. For numerical reasons, the initial value of the specific internal energy of the inflow gas was set to a small nonzero value $\varepsilon_0 = 10^{-6}W_0$. The boundary conditions are $v(1, t) = -v_0$ and the exact solution of ρ at $r = 1$ for all time.

We switched off the gravitational terms in our code and transformed it into a purely special relativistic hydrodynamical code, and have used a grid with 200 equidistant zones. The results displayed in Table 1 and Fig.1, correspond to a particular instant of the evolution after 1000 timesteps. In order to emphasize the relativistic effects, we have done the calculation for a large sample of different initial inflow velocities v_0 . Several conclusions can be established from the data contained in Table 1: i) The postshock density increases with the initial inflow velocity and is unbounded. This is a typical relativistic effect. ii) The ratio ρ^+/W_0 tends to the asymptotic value of 64 when $v_0 \rightarrow 1$, which is consistent with the above asymptotic relations. iii) The maximum of the relative errors for the postshock density, ε_r^{\max} , and the mean relative error of the same

quantity, $\bar{\varepsilon}_r$, are independent of the initial Lorentz factor and converge to 14% and 2%, respectively. This feature of relative errors has been pointed out by Martí and Müller (1995) in discussions of planar shock wall test experiment with their relativistic version of PPM. In the mean relative error we have not considered the zone next to the center, which always dominates the maximum error, due to the well-known effect of numerical overheating. Figure 1 shows our numerical results compared with the analytical ones. The overheating phenomena is less severe by far than the one found by Noh (1987) in his analysis of the corresponding Newtonian problem. Noh (1987) reported errors of the order of 1000% in some of the experiments (in Newtonian hydrodynamics) with artificial viscosity techniques. A maximum relative error of 14% in the postshock density (at the center) is comparable to the one obtained with the Newtonian PPM reported by Noh (1987, see Fig. 24).

IV.2 Spherical accretion onto a black hole

We have tried to reproduce some of the stationary solutions of the *spherical accretion onto a black hole* in two cases: i) *dust* accreting onto a Schwarzschild black hole (Hawley et al. 1984) and ii) an *ideal gas* accreting onto a Schwarzschild black hole (Michel, 1972).

In these tests, the gravitational field is kept fixed. The initial conditions are those of a vacuum, i.e., density is zero everywhere except at the outer boundary where a gas is being continuously injected with a velocity and density given by the exact solution. We have run our code using two different grids of 50 and 100 points, which span the interval $1.05 \leq r/2M \leq 10.0$. Outflow boundary conditions have been taken at the inner boundary $r = 2.1M$.

The analytical solution of a spherical geodesic (*pressureless*) flow accreting onto a black hole can be found in Hawley et al. (1984). Table 2 summarizes relative errors in the three fundamental variables when compared with the analytical solution at a time of $180 M$ (when the stationary solution has been reached). Discrepancies with the exact solution amount to less than 2% for the maximum of the relative errors and less than 1% for the mean relative error. As it should happen these errors decrease under grid refinement (compare first and second rows in Table 2).

The stationary solution of an *ideal gas* accreting spherically onto a Schwarzschild black hole was derived by Michel (1972). A critical point exists, as in the Newtonian description, which can create numerical difficulties. We have considered only solutions of accreting gas having a critical point far outside of our computational domain. Table 2 summarizes the relative errors in the three fundamental variables when compared with the analytical solution at a time of $720 M$, when the stationary solution has been reached. Discrepancies with the exact solution amount to less than 3% for the maximum of the relative errors (less than 1% for the mean relative error). As before, these errors decrease when the grid is refined. Figures 2 and 3 show relativistic rest mass density and the velocity profiles. Three snapshots of quantity D are plotted in Fig. 2 and show that the numerical solution converges to the stationary analytical one. The velocity converges so fast that it's not possible to distinguish the same snapshots in Fig. 3.

As can be deduced from the behaviour of the mean errors under grid refinement (see Table 2), our code is second order accurate for continuous solutions.

IV.3 Detection of the zero value for the fundamental mode against radial oscillations of a compact object

According to the *static stability criterion* (Harrison et al. 1965) it is possible to establish a correlation between the critical points of a curve (in a "gravitational mass versus radius" $M - R$ diagram) built up from equilibrium configurations obeying a given cold EOS and the onset of instability of the zero-frequency mode against radial oscillations. This criterion avoids solving the Sturm-Liouville equation governing radial perturbations of an equilibrium model (see Shapiro and Teukolsky 1983, for a general discussion, or Martí et al. 1988, for details on the numerical solution) A hydro-code should allow for the dynamical study of perturbations over an equilibrium configuration which can be compared with predictions of the static stability criterion. The dynamical detection of a zero in the fundamental mode has been used as a test-bed of hydro-codes by several authors (see, e.g., Ibáñez 1984 and Gourgoulhon 1991). The most accurate results known to the authors are those obtained by Gourgoulhon (1991) using pseudospectral techniques.

In our case we have focussed on a particular critical point, the maximum of the $M - R$ curves corresponding to two kind of compact objects (white dwarfs and neutron stars) which obey suitable EOS (see below) and such that their stability properties have been exhaustively studied (see references below). That maximum separates the curve in two branches, being the stable (unstable) one the corresponding to models having central densities lower (higher) than the critical one.

The calculations of this Section as well as those of Section §IV.5 have been carried out with a numerical grid (which is Eulerian, i.e., fixed) built up in such a way that the radius of the initial model is partitioned into N zones, distributed in geometric progression in order to have finer resolution near the center. In our simulations we have taken $N=330$ and the surface radius $R(t)$ is given by the condition $\rho(R(t)) = \rho(R(t=0)) \approx 10^5 \text{ g/cm}^3$. Hence, the data relative to the initial stellar model are given in the entire grid. As time goes on and, according to the dynamics of each problem, the number of cells covering the star decreases. During the contraction phase of our numerical experiments in this Section (§IV.3), or during the infall epoch of the applications in Section §IV.5, the surface is moved in accordance with the above prescription ($\rho(R(t)) = \rho(R(t=0))$) and we eliminate those cells remaining outside $R(t)$ (in practice, we impose over these cells the vacuum conditions). The important point is that in none of these applications the number of numerical cells used for describing the star are less than 200 (for $N=330$) keeping the numerical resolution in a good level for an accurate calculation. An analogous procedure is established for the expanding phase. Other prescriptions for the surface condition such as, e.g., a combination of moving grids with the integration of the velocity at the surface would be interesting to be studied.

IV.3.1 Detection of a zero in the fundamental mode against radial oscillations of a white dwarf

We have considered a sample of initial models which are white dwarf-like configurations, obtained by solving the stellar structure equations with the equation of state of an ideal gas of electrons including Coulombian corrections due to the ions (Ibáñez, 1984) and with a homogeneous chemical composition (Carbon). The maximum gravitational mass model has a value of $1.3862M_{\odot}$.

We have found a change in the stability behaviour at some point between $1.3847M_{\odot}$ which is a stable model and $1.3853M_{\odot}$ which is an unstable one and collapses in a time which is an order of magnitude higher than the characteristic dynamical one. The corresponding values of the initial central densities are 1.3 and 1.5, respectively, in units of 10^{10}gcm^{-3} .

Figures 4 and 5 show the velocity field as a function of time and radius for, respectively, the stable and unstable models. We point out the different temporal scales involved and the different interval of values spanned by the velocity in each case.

We have also run simulations with a grid of 180 points and taken initial models of constant density. These models are not equilibrium models and, consequently, they start to collapse until some new equilibrium configuration is reached. We find a change in the stability of the models at some point between $1.37M_{\odot}$ and $1.38M_{\odot}$ which is unstable.

IV.3.2 Detection of a zero in the fundamental mode against radial oscillations of a neutron star

We have considered a family of neutron stars obeying the EOS derived by Diaz-Alonso (1985) in a field theoretical model approach to neutron matter at zero and finite temperature (Diaz-Alonso et al 1989).

The model describes a many-body system of mutually interacting nucleons and mesons: a fictitious σ particle, pions, ρ and ω mesons. The interaction is given by a relativistic Lagrangian containing the free Dirac Lagrangian for the nucleons, the Lagrangians for the σ particle, pion and ω and ρ mesons. The interaction is described by two pieces: one containing the meson-nucleon interaction in the form of Yukawa-like couplings, and one which describes the meson-meson interaction. The attractive part of the nuclear interaction is provided by the σ and pion exchange. The ω and ρ mesons give rise to a repulsive short-range interaction, which is charge-dependent in the latter case, in such a way that the EOS behaviour is different for nuclear symmetric matter as for pure neutron matter. Details on the solution of the model can be found in the references above.

We will focuss on the EOS II in Diaz-Alonso (1985) which was derived fitting the free parameters in the Lagrangian in such a way that, for symmetric nuclear matter, the model saturates at a density $\rho_n = 2.837 \times 10^{14} \text{ gcm}^{-3}$. The corresponding binding energy is -15.68 MeV, the symmetry energy 33.17 MeV, and the nuclear incompressibility is $K = 225$ MeV.

The equilibrium configurations obeying this EOS at zero temperature have been taken as initial models in our hydro-code. Their macroscopic properties were exhaustively stud-

ied in Diaz-Alonso and Ibáñez (1985) for the cold version of EOS II. The maximum gravitational mass is $1.94556M_{\odot}$ which corresponds a central energy density of $2.48 \times 10^{15} \text{ gcm}^{-3}$. The reader interested on the properties of stability against radial oscillations and the equilibrium features of slowly rotating stars obeying the hot version of that EOS can address, respectively, to Martí et al. (1988) and Romero et al. (1992).

We have generated a perturbation of the equilibrium models by imposing an initial velocity profile according to the law $v(r) = -v_o(r/R)$. This procedure has the advantage of allowing a clear distinction between the dynamics of the models, erasing round-off errors induced in the numerical construction of the initial model (for the hydro-code) from the model generated by solving the structure equations. As before, the value of $R(t)$ is obtained from the condition: $\rho(R(t)) = \rho(R(t=0))$.

Taking a value for v_o of 10^{-3} we have found a change in the stability behaviour between the model of $1.94532M_{\odot}$ (central density: $2.55 \times 10^{15} \text{ gcm}^{-3}$), which is stable, and the model $1.94518M_{\odot}$ (central density: $2.57 \times 10^{15} \text{ gcm}^{-3}$), which is unstable. Unlike the stable configuration –which undergoes a oscillating motion– the unstable one collapses in a time of the order of the characteristic dynamical time. The behaviour of the rest-mass density, as a function of time, can be seen in Figs. 6 and 7 for, respectively, the stable and unstable models. In these figures we have selected a sample of mass shells by making a equipartition of the total gravitational mass in eleven shells of the same width and plotted the ten inner ones. For the values of the central density involved in this study, the dynamical characteristic time is of about ≤ 0.8 msec, which is interesting in view of the different temporal scales which govern the dynamics of both models. The stable configuration (Fig. 6) displays a plateau profile during more than 5 times its dynamical characteristic time. The unstable configuration (Fig. 7) starts to collapse in a characteristic time less than two times its dynamical characteristic time.

IV.4 Oppenheimer-Snyder collapse

The gravitational collapse (into a black hole) of a homogeneous spherical dust cloud ($p=0$) has been exhaustively studied since the original paper of Oppenheimer and Snyder (1939). Depending on the particular time slicing and coordinate gauge used simple analytical expressions are available for both the metric coefficients and the matter variables (Petrich et al., 1985, 1986). The solution to this problem in the RGPS (as in the present work) can be found in Petrich et al. (1986) and Gourgoulhon (1992,1993). We have summarized these previous theoretical works in an appendix. Since during the last epoch of Oppenheimer-Snyder collapse, the variables involved (both the geometrical and hydro-dynamical) reach extreme values, it is generally considered a good test-bed calculation for fully general-relativistic time-dependent numerical codes (Petrich et al., 1985, 1986; Gourgoulhon, 1992,1993; Baumgarte et al., 1994). Hence, we have used it as a check of our code in the case of strong gravitational fields, as well as ultrarelativistic velocities. Although no shocks appear during the evolution of the pressureless ball, very steep spatial and temporal gradients develop at the last stages of its evolution.

Results of our simulations have been plotted together with the exact solution in Figs. 8-10, as a function of radial coordinate, normalized to the Schwarzschild radius of the initial configuration, for a sample of values of the temporal coordinate labelled from 0 to 6 (see the corresponding captions). Figure 8 shows the rest-mass density, normalized to its initial value. Due to the gauge used, the existence of a positive spatial gradient of rest-mass density is noticeable. Figure 9 displays the behaviour of the physical velocity. As expected, the velocity of the surface tends to unity as the collapse proceeds to its late stage, having a minimum value of about $v = -0.92$ (plotted in Fig. 9). The geometrical quantity α is plotted in Fig. 10. At the late epoch we have succeeded in reaching a value as low as 1.3232×10^{-10} .

In this application the position of the surface $R(t)$ is defined by the analytical solution. Note that due to our procedure for moving the surface the value corresponding to this point (the last numerical cell) suffers of an error. This error is associated to the fact that our grid is Eulerian making difficult to precise the exact position of the surface. A comoving grid would allow to solve the surface with more accuracy and would result in spatial gradients steeper than those displayed in Figs. 8-10.

Figures 11 show in a space-time diagram the trajectories of the different mass shells in terms of the proper time (Fig. 11a) and the coordinate time (Fig. 11b). The effect of freezing in the evolution of the system is noticeable from Fig. 11a, by comparison with Fig. 11b. Our calculation has evolved to an epoch later than that reached by Gourgoulhon (1992) with the pseudospectral technique. The results displayed in Figs. 8-11 confirm the powerful capabilities of our numerical techniques for treating steep spatial and temporal gradients.

IV.5 An application to the stellar core collapse

A very simple way of modelling the essential features of stellar core collapse in massive stars is to incorporate a simple equation of state into a hydro-code, like that of an ideal gas, but taking an adiabatic exponent which can depend on density according to a particular prescription. The EOS we have used is a Γ -law such that Γ varies with density according to:

$$\Gamma = \Gamma_{min} + \eta(\log \rho - \log \rho_b) \quad , \quad (40)$$

with: $\eta = 0$ if $\rho < \rho_b$ and $\eta > 0$ otherwise (Van Riper, 1979).

Two set of values for the parameters Γ_{min} , η and ρ_b have been considered: $\{1.33, 1, 2.5 \times 10^{14} \text{ gcm}^{-3}\}$ (*model A*) and $\{1.33, 5, 2.5 \times 10^{15} \text{ gcm}^{-3}\}$ (*model B*). Model A exhibits standard values of the parameters, i.e., the effective adiabatic exponent of infalling material and the value of nuclear density (for symmetric nuclear matter at zero temperature) at the saturation point. Model B is rather exotic due to the particular values for the bounce density and stiffness $\eta = 5$; however, we have considered this model in order to check the ability of our hydro-code in solving numerically flows which develop strong shocks in very strong gravitational fields.

The initial model in the present application is a white dwarf having a gravitational mass of $1.3862 M_\odot$ corresponding to the maximum mass cited in the section before.

We have run models A and B with a grid of 330 points distributed – as in the previous application – in a geometric progression (in the following, figures are numbered with a number followed by a or b corresponding, respectively, to cases A and B). The solution converges quickly by taking different grids. No relevant differences were found in the numerical results when the number of points is increased from 330 points to 630 grid points. Poor grids lead to results which differ from the converged ones, but the essential features of the shock remain sharply solved, in typically two numerical cells. This property is one of the most relevant of these numerical techniques. As in Section §IV.3 the value of $R(t)$ is obtained from the condition: $\rho(R(t)) = \rho(R(t = 0))$.

Table 3 shows the main features of both models during the *infall epoch*. Important numbers are those corresponding to the maximum of velocity, that is, 0.41 and 0.62, respectively, for cases A and B (see also Figs. 12). Also, it is interesting to point out the particular values of the geometric factor α^2 at the maximum compression and to compare them with those corresponding at the surface of a typical neutron star ≈ 0.75 .

The kinetic energy of the material ejected has been calculated at different times, those corresponding to some fixed values for the position of the shock in our Eulerian frame. Table 4 displays the main features of both models during the *prompt phase*. Case B is globally more energetic than case A. The ulterior evolution after the shock has arrived at the surface has not been followed up in the present work.

Note the behaviour of the velocity field as it can be seen in Figs. 12. The shock is sharply solved in one or two zones and is free of spurious oscillations. In these figures, labels stand for the temporal sequence of each curve (see the corresponding table caption). From Figs. 12 we can see that the radius of the inner core, at the time of maximum compression and for which the infall velocity is maximum (see Table 3) and the shock has been formed, is 12.6 km. At the corresponding time in case B, the size is only 6.3 km. This strong difference together with other elements such as the particular values of the velocity and the low values of the geometric factor α^2 (see Table 3) are the signatures of the fact that general relativistic effects are more important in case B than in case A.

Rest-mass density, as a function of radial coordinate, for several times is plotted in Figs. 13. The propagation of the shock can be followed in this figure. Qualitatively, case B displays the same behaviour. The jump in density is of about one order of magnitude. The maximum values of the central density differ in both cases by a factor of five (see Table 3).

Figures 14 show several snapshots of the internal specific energy (in units of c^2) as a function of radial coordinate. The shock is sharply solved and its propagation is well defined there. Note the huge values of the internal energy reached at the center (curve labelled by 3 in Figs. 14) of ≈ 0.18 (case A), being ≈ 0.42 in case B.

The conservative features of our hydro-code, consistent with the conservation laws of baryonic mass and gravitational mass (or binding energy), are displayed in Figs. 15 and 16. Figures 15 show several snapshots of the gravitational mass, as a function of radial coordinate. The binding energy has been plotted, as a function of radial coordinate, in Figs. 16. In both figures, curves labelled by 1 correspond to the initial model, and the ones labelled by 3 to the time of maximum compression. A glance at these figures gives

confidence in the conservative features of the code, since the relative errors at the surface are consistent with the accuracy of our algorithm. Let us focus on those curves labelled by 3: Case A generates an inner core (the seed of the protoneutron star) which has a mass and radius greater than those corresponding to case B. The size in mass of the inner core at the time of maximum compression is $\approx 1.15M_{\odot}$ and $\approx 1.0M_{\odot}$ for cases A and B, respectively. The total binding energy of the initial model is, in units of $M_{\odot}c^2$, -3.1×10^{-4} . Conservation of binding energy is preserved by our code.

We have built up spacetime diagrams in order to simplify the understanding of the evolution and, eventually, to compare with other calculations. Figs. 17 show the areal radii which enclose a sample of mass shells (see captions of these figures) in terms of the time coordinate. Unlike the Oppenheimer-Snyder case (Fig. 11a), in Figs. 17 is very remarkable the existence of an absolute minimum of the radius enclosing a given mass, as well as the propagation of the shock. From these figures we can distinguish between the inner core which reaches hydrostatic equilibrium and the outer part which is ejected with a kinetic energy greater than 4×10^{51} erg (7×10^{51} erg) in case A (B) when the shock is at 560 km (see table 4).

Finally, to emphasize the importance of general relativistic effects we plot (in Figs. 18) the geometrical quantity α^2 as a function of radial coordinate and at several times of its evolution. As can be seen from Figs. 18, α^2 is a continuous function throughout the shock. The curve labelled 2 corresponds to the time at which the absolute minimum is reached at the center, being 0.49 and 0.14 for cases A and B, respectively.

VII. CONCLUSIONS

In this work we have described a full general relativistic one-dimensional hydrodynamical code which incorporates a modern high-resolution shock-capturing algorithm for the correct modelling of formation and propagation of strong shocks. Strong shocks are sharply solved. Our algorithm is conservative, monotone and upwind. It makes use of a linearized Riemann solver. The present version of our hydro-code has the fundamental property of conservation of those quantities (such as the baryonic mass and the total energy) whose evolution is described by continuity-like equations.

We have carried out several numerical tests and applications of our code. They have been selected in order to check a large range of different properties: special relativistic effects, geometrical effects, general relativistic effects in a background or fully general relativistic dynamics. In particular, the spherical shock reflection problem has been solved in the ultrarelativistic regime most successfully. We have reproduced some of the stationary solutions describing a flow evolving in a given background. We have compared dynamical study of perturbations with the static stability criterion of equilibrium configurations. Oppenheimer-Snyder collapse has given the opportunity to check our code with the analytical solution of a fully dynamical spacetime. Finally, we have made a simple application to the dynamics of the collapse of compact objects using a simple microphysics. Case B of this last application displays strong shocks evolving in presence of gravitational fields so huge that the coupling introduced by the geometrical quantities makes the system to be

solved a highly nonlinear system. Hence, the severity of some of the tests that our code has overcome lead us to be confident in the quality of the results in future applications.

Let us give some examples of the astrophysical applications that we are envisaging. First, we are interested in carrying out simulations of collapsing stellar cores with a realistic initial model and an updated microphysics. The influence of the gravitational field in the formation and propagation of relativistic fireballs – considered as good candidates for modelling γ -ray bursts – will also be studied with the hydro-code analyzed in present paper.

ACKNOWLEDGMENTS

This work has been supported by the Spanish DGICYT (grant PB91-0648) and a grant from the IVEI. José M^a. Martí has benefited from a european postdoctoral fellowship (contract number ERBCHBICT930496). Calculations were carried out in a VAX 6000/410 at the Instituto de Física Corpuscular and in a IBM 30-9021 VF at the Centre d'Informàtica de la Universitat de València. Authors acknowledge to an anonymous referee for his useful comments and suggestions and to Dr. Carinhas for his careful reading of the manuscript.

Appendix A. Oppenheimer-Snyder collapse in RGP_S coordinates

The gravitational collapse of a homogeneous and pressureless ball of dust, initially at rest (Oppenheimer and Snyder, 1939), has been proposed as a test-bed for fully general-relativistic codes. Let us summarize in this appendix the analytical results of this problem when they are expressed in terms of the RGP_S coordinates (Petrich et al. 1986, Gourgoulhon 1993).

According to Petrich et al. (1986), the solution consists of finding coordinate transformations from the canonical forms of the interior Friedmann –closed– and the exterior Schwarzschild metrics.

The closed Friedmann metric is

$$ds^2 = -d\tau^2 + a(\tau)^2 \left(d\chi^2 + \sin^2 \chi (d\theta^2 + \sin^2 \theta d\phi^2) \right) , \quad (41)$$

where τ is the proper time of the fluid and χ varies into the interval $0 \leq \chi \leq \chi_s$, $\chi = 0$ and χ_s being, respectively, the values of χ at the center and at the surface of the star. χ_s can be determined from the gravitational mass of the cloud M and its initial radius $R(0)$:

$$\chi_s = \arcsin \left(\frac{2M}{R(0)} \right)^{1/2} . \quad (42)$$

In terms of the conformal time η , defined by the relation

$$\frac{d\eta}{d\tau} = \frac{1}{a(\tau)} , \quad (43)$$

the metric (41) can be written

$$ds^2 = a(\eta)^2 \left(-d\eta^2 + d\chi^2 + \sin^2 \chi (d\theta^2 + \sin^2 \theta d\phi^2) \right) . \quad (44)$$

The exterior metric is given by the well-known Schwarzschild solution for vacuum

$$ds^2 = - \left(1 - \frac{2M}{r} \right) dt^2 + \left(1 - \frac{2M}{r} \right)^{-1} dr^2 + r^2 (d\theta^2 + \sin^2 \theta d\phi^2) . \quad (45)$$

The RGPS form of the interior metric is given by Eq. (3).

The solution of the Oppenheimer-Snyder in the RGPS spacetime can be derived in, basically, two steps: i) First, the interior Friedmann metric (44) has to be transformed into RGPS coordinates (3). ii) Second, interior and exterior solutions have to be appropriately matched at the surface of the star.

The explicit expressions we were looking for are:

1) *Coordinate transformations:*

$$t = 2M \left[\frac{1}{\tan \chi_s} \left(\eta_s + \pi + \frac{1}{2 \sin^2 \chi_s} (\eta_s + \pi - \sin \eta_s) \right) + \ln \left(\frac{\tan(\eta_s/2) - \tan \chi_s}{\tan(\eta_s/2) + \tan \chi_s} \right) \right] , \quad (46)$$

where $\eta_s = \eta_s(\eta_c) = -2 \arccos \left(\frac{\cos(\eta_c(t)/2)}{\cos^{1/2} \chi_s} \right)$, and $\eta_c = \eta_c(t)$ being the value of η at $\chi = 0$ on the hypersurface Σ_t ($t=\text{constant}$). The above equation allows to obtain –by inverting it– the function $\eta_c(t)$.

The radius at the surface satisfies:

$$R(t) = R(0) \left(1 - \frac{\cos^2(\eta_c(t)/2)}{\cos \chi_s} \right) \quad (47)$$

The function $\chi(t, r)$ is implicitly defined by:

$$r = R(0) \left(1 - \frac{\cos^2(\eta_c(t)/2)}{\cos \chi} \right) \frac{\sin \chi}{\sin \chi_s} \quad (48)$$

2) *Geometric quantities:*

$$\alpha(r, t) = \begin{cases} \alpha_o(\eta_c, \chi_s) \frac{\cos \chi - \cos^2(\eta_c/2)}{(\cos^3 \chi - \cos^2(\eta_c/2))^{1/2}} & \text{if } 0 \leq r \leq R(t) \\ \left(1 - \frac{2M}{r} \right)^{1/2} & \text{if } r \geq R(t) \end{cases}$$

$$X(r, t) = \begin{cases} \left(\frac{\cos \chi - \cos^2(\eta_c/2)}{\cos^3 \chi - \cos^2(\eta_c/2)} \right)^{1/2} & \text{if } 0 \leq r \leq R(t) \\ \left(1 - \frac{2M}{r} \right)^{-1/2} & \text{if } r \geq R(t) \end{cases}$$

where

$$\alpha_o(\eta_c, \chi_s) \equiv \frac{\cos^3 \chi_s - \cos^2(\eta_c/2)}{(\cos \chi_s - \cos^2(\eta_c/2))^{3/2}} \quad (49)$$

3) *Matter variables:*

$$v(r, t) = -\frac{\cos(\eta_c/2) \tan \chi}{(\cos \chi - \cos^2(\eta_c/2))^{1/2}} \quad (50)$$

$$\rho(r, t) = \frac{3 \sin^6 \chi_s}{32\pi M^2} \left(\frac{\cos \chi}{\cos \chi - \cos^2(\eta_c/2)} \right)^3 \quad (51)$$

References

- [1] Anile, A.M., 1989, in *Relativistic fluids and magneto-fluids*, Cambridge University Press
- [2] Arnowitt, R., Deser, S., and Misner, C.W., 1962, in *Gravitation*, ed. by Witten, L., Wiley
- [3] Baumgarte, T.W., Shapiro, S.L., and Teukolsky, S.A., 1995, *ApJ*, **443**, 717.
- [4] Bethe, H., Wilson, J. R., 1985, *ApJ*, **295**, 14
- [5] Bonazzola, S., and Marck, J.A., 1991, *J. Comp. Phys.*, **97**, 535
- [6] Bondi, H., 1964, *Proc. Royal Soc. of London*, **A281**, 39
- [7] Centrella, J., and Wilson, J. R., *ApJ Suppl. Ser.*, 1984, **54**, 229
- [8] Colella, P., and Woodward, P.R., *J. Comp. Phys.*, 1984, **54**, 174
- [9] Courant, R., and Friedrichs, K.O., 1948, "Supersonic Flows and Shock Waves", (Interscience)
- [10] Diaz-Alonso, J., 1985, *Phys. Rev.*, **D 31**, 1315.
- [11] Diaz-Alonso, J., and Ibáñez, J. M., 1985, *ApJ*, **291**, 308.
- [12] Diaz-Alonso, J., Ibáñez, J. M., and Sivak, H., 1989, *Phys.Rev.*, **C 39**, 671.
- [13] Eulderink, F., 1993, Ph.D.Thesis, Sterrewacht Leiden
- [14] Evans, C. R., in "Dynamical space-times and numerical relativity", ed. by J. Centrella (Cambridge University Press, 1986)
- [15] Font, J.A., Ibáñez, J.M., Marquina, A., and Martí, J.M., 1994, *A&A*, **282**, 304
- [16] Gingold, R.A., and Monaghan, J.J., 1977, *MNRAS*, **181**, 375
- [17] Gottlieb, D., and Orszag, S., 1977, *Numerical Analysis of Spectral Methods.: Theory and Application*, Regional Conference Series Lectures in Applied Mathematics, **26** (SIAM, Philadelphia,1977)
- [18] Gourgoulhon, E., 1991, *A&A*, **252**, 651
- [19] Gourgoulhon, E., 1992, Ph.D. Thesis, Université de Paris VII
- [20] Gourgoulhon, E., 1993, *Ann. Phys. Fr.*, **18**, 1.
- [21] Harrison, B.K., Thorne, K.S., Wakano, M., and Wheeler, J.A., 1965, *Gravitation Theory and Gravitational Collapse*, Chicago University Press.

- [22] Hawley, J.F., Smarr, L.L., and Wilson, J.R., 1984, *Ap. J. Suppl.*, **55**, 211
- [23] Herant, M., Benz, W., Hix, W.R., Fryer, Ch.L., and Colgate, S.A., 1994, *ApJ*, **435**, 339
- [24] Ibáñez, J.M.^a., 1984, *A&A*, **135**, 382
- [25] Ibáñez, J.M.^a., Martí, J.M.^a., Miralles, J.A., and Romero, V., 1992, in *Approaches to Numerical Relativity*, ed. by D'Inverno, Cambridge University Press
- [26] Ibáñez, J.M.^a., 1993, in *Rotating Objects and Relativistic Physics*, ed. by Chinea, F.J., and González-Romero, L.M., Series Lecture Notes in Physics, **423**, 149 (Springer-Verlag)
- [27] Janka, H.-Th., and Müller, E., 1993, in *Frontiers of Neutrino Astrophysics* (Universal Academy Press: Tokyo)
- [28] Lax, P., 1972, *Regional Conference Series Lectures in Applied Math.*, **11** (SIAM, Philadelphia)
- [29] LeVeque, R.J., 1992, in *Numerical Methods for Conservation Laws*, Birkhäuser.
- [30] Lucy, L.B., 1977, *Astron. J.*, **82**, 1013
- [31] Mann, P.J., 1991, *Comput. Phys. Comm.*, **67**, 245
- [32] Marquina, A., Martí, J.M.^a., Ibáñez, J.M.^a., Miralles, J.A., and Donat, R., 1992, *A&A*, **258**, 566
- [33] Martí, J. M.^a., Miralles, J. A., Diaz-Alonso, J., and Ibáñez, J. M.^a., 1988, *ApJ*, **329**, 780.
- [34] Martí, J.M.^a., Ibáñez, J.M.^a., and Miralles, J.A., 1991, *Phys. Rev.*, **D43**, 3794
- [35] Martí, J.M.^a., and Müller, E., 1994, *J. Fluid Mech.*, **258**, 317
- [36] Martí, J.M.^a., and Müller, E., 1995, *J. Comp. Phys.*, *in press*.
- [37] Martí, J.M.^a., Müller, E., Font, J.A., and Ibáñez, J.M.^a., 1995a, *ApJ Lett.*, *in press*
- [38] Martí, J.M.^a., Müller, E., Font, J.A., Ibáñez, J.M.^a., and Marquina, A., 1995b *in preparation*
- [39] May, M.M., and White, R.H., 1967, *Math. Comp. Phys.*, **7**, 219
- [40] Mészáros, P., Laguna, P., and Rees, M.J., 1993, *ApJ*, **415**, 181
- [41] Michel, F.C., 1972, *Ap. Space Sci.*, **15**, 153
- [42] Nakamura, T., *Prog. Teor. Phys.*, 1981, **65**, 1876

- [43] Nakamura, T., Maeda, K., Miyama, S., and Sasaki, M., *Prog. Teor. Phys.*, 1980, **63**, 1229
- [44] Nakamura, T., and Sato, H., *Prog. Teor. Phys.*, 1982, **67**, 1396
- [45] Noh, W.F., 1987, *J. Comp. Phys.*, **72**, 78.
- [46] Norman, M.L., and Winkler, K-H.A., 1986, in *Astrophysical Radiation Hydrodynamics*, ed. by Norman, M.L., and Winkler, K-H.A. (Reidel).
- [47] Oppenheimer, J.R., and Snyder, H., 1939, *Phys.Rev.*, **56**, 455.
- [48] Petrich, L.I., Shapiro, S.L., and Teukolsky, S.A., 1985, *Phys.Rev.*, **D31**, 2459.
- [49] Petrich, L.I., Shapiro, S.L., and Teukolsky, S.A., 1986, *Phys.Rev.*, **D33**, 2100.
- [50] Petrich, L.I., Shapiro, S.L., Stark, R.F., and Teukolsky, S.A., 1989, *ApJ*, **336**, 313
- [51] Piran, T., *J. Comp. Phys.*, 1980, **35**, 254
- [52] Piran, T., Shemi, A., and Narayan, R., 1993, *MNRAS*, **263**, 861.
- [53] Romero, J.V., Diaz-Alonso, J., Ibáñez, J.M., Miralles, J.A., and Pérez, A., 1992, *ApJ*, **395**, 612.
- [54] Schneider, V., Katscher, V., Rischke, D.H., Waldhauser, B., Marhun, J.A., and Munz, C.-D., 1993, *J. Comput. Phys.*, **105**, 92.
- [55] Shapiro, S.L., and Teukolsky, S.A., 1983, *Black Holes, White Dwarfs and Neutron Stars*, John Wiley.
- [56] Stark, R. F., and Piran, T., *Comp. Phys. Rept.*, 1987, **5**, 221
- [57] Swesty, F.D., Lattimer, J.M., and Myra, E.S., 1994, *ApJ.*, **425**, 195
- [58] Van Leer, B., 1979, *J. Comp. Phys.*, **32**, 101.
- [59] Van Riper, K.A., 1979, *ApJ*, **232**, 558
- [60] Wilson, J. R., 1972, *ApJ*, **173**, 431
- [61] Wilson, J. R., in *"Sources of gravitational radiation* , ed. L. L. Smarr (Cambridge University Press, 1979)

Table 1
Relativistic spherical shock reflection

v_0	W_0	ρ^+	ε_r^{\max}	$\bar{\varepsilon}_r$
0.1	1.005	342	0.088	0.016
0.9	2.3	343	0.090	0.015
0.99	7.1	614	0.11	0.018
0.999	22	1580	0.13	0.020
0.9999	71	4671	0.14	0.021
0.99999	224	14455	0.14	0.021
0.999999	707	45399	0.14	0.022
0.9999999	2236	143252	0.14	0.022

Initial inflow velocity is $-v_0$ (in units of the speed of light) corresponding to an initial Lorentz factor W_0 . Maximum and mean relative errors of the postshock density, ε_r^{\max} and $\bar{\varepsilon}_r$ (after 1000 timesteps).

Table 2
Spherical accretion onto a black hole

<i>EOS</i>	<i>Grid</i>	D		S		τ	
		ε^{\max}	$\bar{\varepsilon}$	ε^{\max}	$\bar{\varepsilon}$	ε^{\max}	$\bar{\varepsilon}$
Dust ($p=0$)	50	0.020	0.008	0.020	0.009	0.022	0.010
	100	0.006	0.002	0.006	0.002	0.007	0.003
Ideal gas	50	0.021	0.009	0.030	0.010	0.033	0.012
	100	0.006	0.002	0.009	0.003	0.010	0.003

Maximum and mean relative errors of the numerical solution, ε^{\max} and $\bar{\varepsilon}$ (at a time 720 M). *EOS*: equation of state.

Table 3**Features of the stellar collapse: infall epoch**

Model	ρ_{14}^{max}	$-v_{max}$	α_{min}^2
<i>A</i>	7.28	0.41	0.49
<i>B</i>	34.6	0.62	0.14

ρ_{14}^{max} is the maximum of central density at the infall epoch (in units of 10^{14} gcm $^{-3}$).
 $-v_{max}$ is the maximum of velocity at the infall epoch (in units of the speed of light).
 α_{min}^2 is the minimum of the purely temporal component of the metric tensor at the infall epoch.

Table 4**Features of the stellar collapse: prompt phase**

Model	KE_1	KE_2	KE_3
<i>A</i>	1.26	3.18	4.53
<i>B</i>	1.18	4.93	7.11

KE_i kinetic energy of the material reaching escape velocities, when the shock is at the position r_i ($=100, 240, 560$ km., respectively). Energies are given in units of 10^{51} erg.

Figure captions

Figure 1.- Relativistic spherical shock reflection. We use a continuous line for the exact solution and different symbols like a plus, a diamond and a triangle for velocity (in units of the speed of light), density and specific internal energy, respectively.

Figure 2.- Spherical accretion of dust onto a Schwarzschild black hole. Snapshots of the relativistic mass density, in logarithmic scale and geometrized units, as a function of the radial coordinate (in units of the mass of the black hole)

Figure 3.- Spherical accretion of dust onto a Schwarzschild black hole. Velocity versus the radial coordinate (in units of the mass of the black hole) at a particular time.

Figure 4.- Velocity profile as a function of radial coordinate and time for a stable white-dwarf.

Figure 5.- Velocity profile as a function of radial coordinate and time for an unstable white-dwarf.

Figure 6.- Rest-mass density as a function of time for a stable model of neutron star having $M = 1.94532M_{\odot}$ and a central density of $2.55 \times 10^{15} \text{ g/cm}^3$. Each curve corresponds to the following mass shells: $m_j = (M/11) \times j$ ($j = 1, \dots, 10$)

Figure 7.- Rest-mass density as a function of time for an unstable model of neutron star having $M = 1.94518M_{\odot}$ and a central density of $2.57 \times 10^{15} \text{ g/cm}^3$. Each curve corresponds to the following mass shells: $m_j = (M/11) \times j$ ($j = 1, \dots, 10$)

Figure 8.- Snapshots of the rest-mass density (normalized to the initial value) as a function of the radial coordinate (normalized to $2M$) for the Oppenheimer-Snyder collapse. Labels stand, respectively, for the following values of time (in msec.): 0, 0.155, 0.189, 0.206, 0.218, 0.228 and 0.430

Figure 9.- Snapshots of the velocity as a function of the radial coordinate (normalized to $2M$) for the Oppenheimer-Snyder collapse. Labels stand, respectively, for the following values of time (in msec.): 0, 0.155, 0.189, 0.206, 0.218, 0.228 and 0.430

Figure 10.- Snapshots of the lapse as a function of the radial coordinate (normalized to $2M$) for the Oppenheimer-Snyder collapse. Labels stand, respectively, for the following values of time (in msec.): 0, 0.155, 0.189, 0.206, 0.218, 0.228 and 0.430

Figure 11a.- Spacetime diagram for the Oppenheimer-Snyder collapse. Trajectories of a sample of mass shells in a proper time (in msec.) versus radial coordinate (normalized to $2M$). Each curve corresponds to the following mass shells: $m_j = (M/11) \times j$ ($j = 1, \dots, 10$)

Figure 11b.- Spacetime diagram for the Oppenheimer-Snyder collapse. Trajectories of a sample of mass shells in a coordinate time (in msec.) versus radial coordinate (normalized to $2M$) diagram. Each curve corresponds to the following mass shells: $m_j = (M/11) \times j$ ($j = 1, \dots, 10$)

Figure 12a.- Snapshots of the velocity profile as a function of the radial coordinate (model A). Labels stand, respectively, for the following values of time (in msec.): 80.49, 80.74, 80.91, 81.04, 81.20, 81.39, 81.76, 81.94, 82.86, 84.25 and 86.12

Figure 12b.- Snapshots of the velocity profile as a function of the radial coordinate (model B). Labels stand, respectively, for the following values of time (in msec.): 80.68, 80.79, 80.93, 81.06, 81.25, 81.33, 81.76, 82.47, 83.22, 84.73 and 86.51

Figure 13a.- Snapshots of the rest-mass density profile as a function of the radial

coordinate (model A). Labels stand , respectively, for the following values of time (in msec.): 80.49, 80.91, 81.20, 81.76, 82.86 and 86.12

Figure 13b.- Snapshots of the rest-mass density profile as a function of the radial coordinate (model B). Labels stand , respectively, for the following values of time (in msec.): 80.68, 80.93, 81.25, 81.76, 83.22 and 86.51

Figure 14a.- Snapshots of the specific internal energy profile as a function of the radial coordinate (model A). Labels stand , respectively, for the following values of time (in msec.): 80.49, 80.74, 80.91, 81.04, 81.20, 81.39, 81.76, 81.94, 82.86, 84.25, and 86.12

Figure 14b.- Snapshots of the specific internal energy profile as a function of the radial coordinate (model B). Labels stand , respectively, for the following values of time (in msec.): 80.68, 80.79, 80.93, 81.06, 81.25, 81.33, 81.76, 82.47, 83.22, 84.73 and 86.51

Figure 15a.- Snapshots of the gravitational mass profile as a function of the radial coordinate (model A). Labels stand , respectively, for the following values of time (in msec.): 0, 80.49, 80.91, 81.20, 81.76, 82.86 and 86.12

Figure 15b.- Snapshots of the gravitational mass profile as a function of the radial coordinate (model B). Labels stand , respectively, for the following values of time (in msec.): 0, 80.68, 80.93, 81.25, 81.76, 83.22 and 86.51

Figure 16a.- Snapshots of the binding energy profile as a function of the radial coordinate (model A). Labels stand , respectively, for the following values of time (in msec.): 0, 80.49, 80.91, 81.20, 81.76, 82.86 and 86.12

Figure 16b.- Snapshots of the binding energy profile as a function of the radial coordinate (model B). Labels stand , respectively, for the following values of time (in msec.): 0, 80.68, 80.93, 81.25, 81.76, 83.22 and 86.51

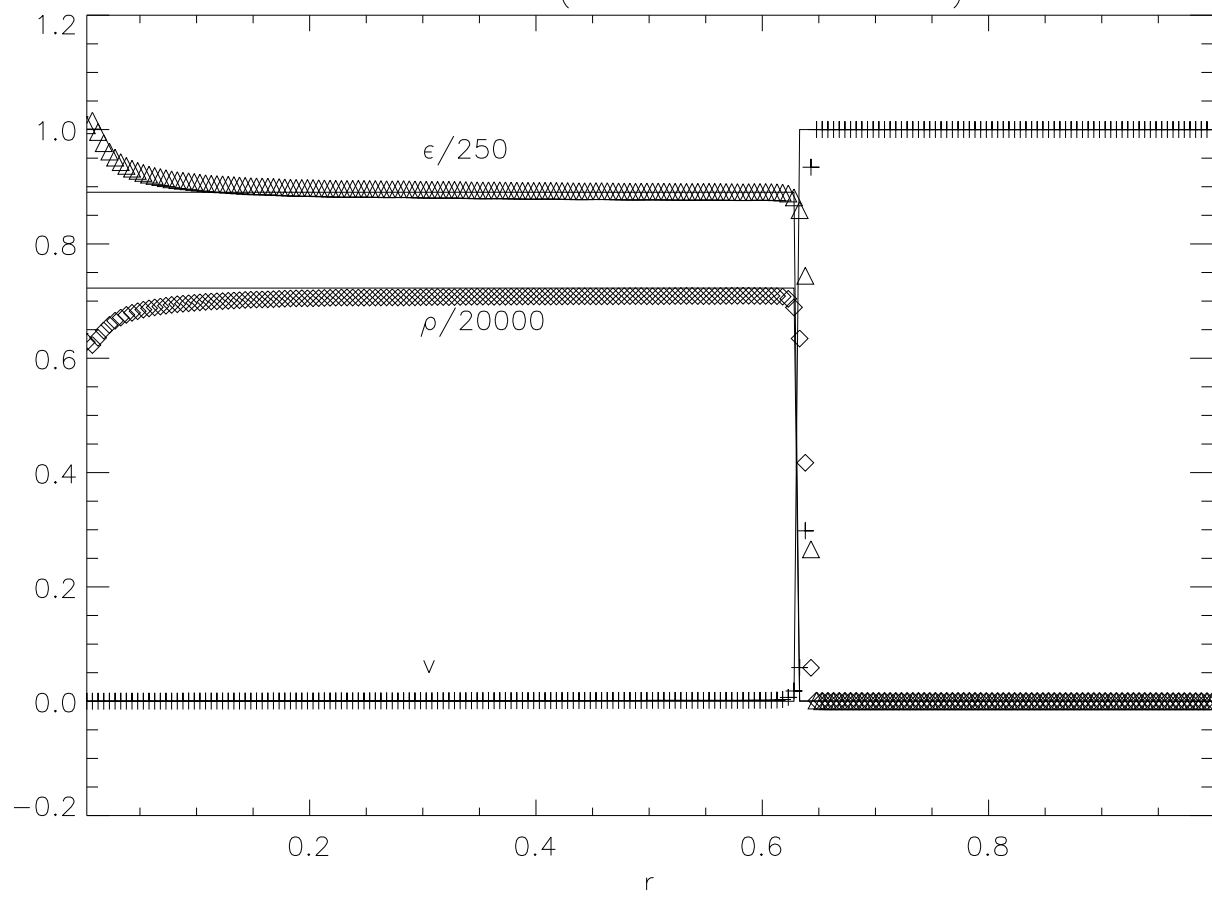
Figure 17a.- Spacetime diagram for model A. Trajectories of a sample of mass shells in a proper time (in msec.) versus radial coordinate (in km. and logarithmic scale). Each curve corresponds to the following mass shells: $m_j = (M/11) \times j$ ($j = 1, \dots, 10$)

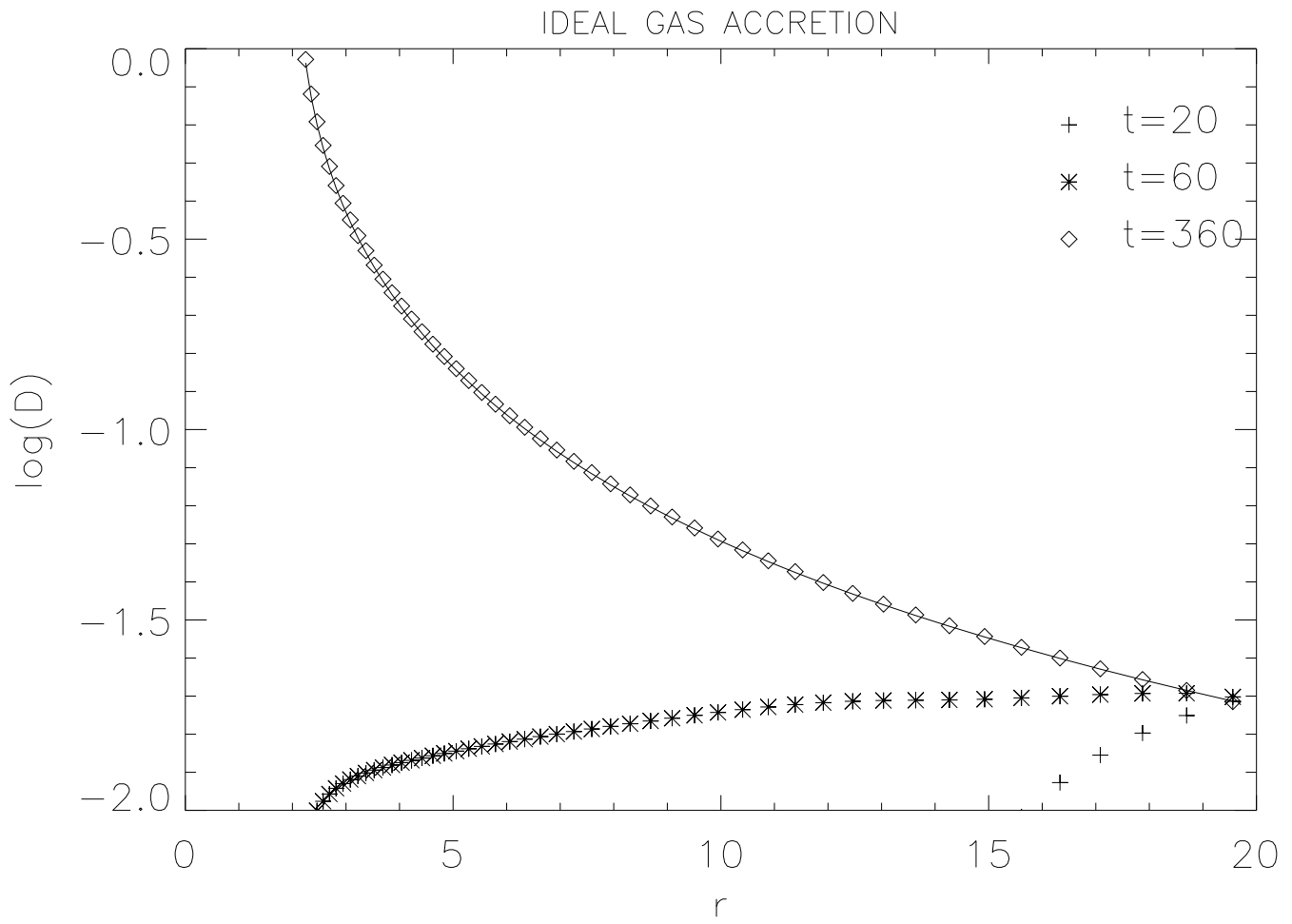
Figure 17b.- Spacetime diagram for model B. Trajectories of a sample of mass shells in a proper time (in msec.) versus radial coordinate (in km. and logarithmic scale). Each curve corresponds to the following mass shells: $m_j = (M/11) \times j$ ($j = 1, \dots, 10$)

Figure 18a.- Snapshots of the geometrical quantity α^2 as a function of the radial coordinate (model A). Labels stand , respectively, for the following values of time (in msec.): 80.49, 80.91, 81.76, and 86.12

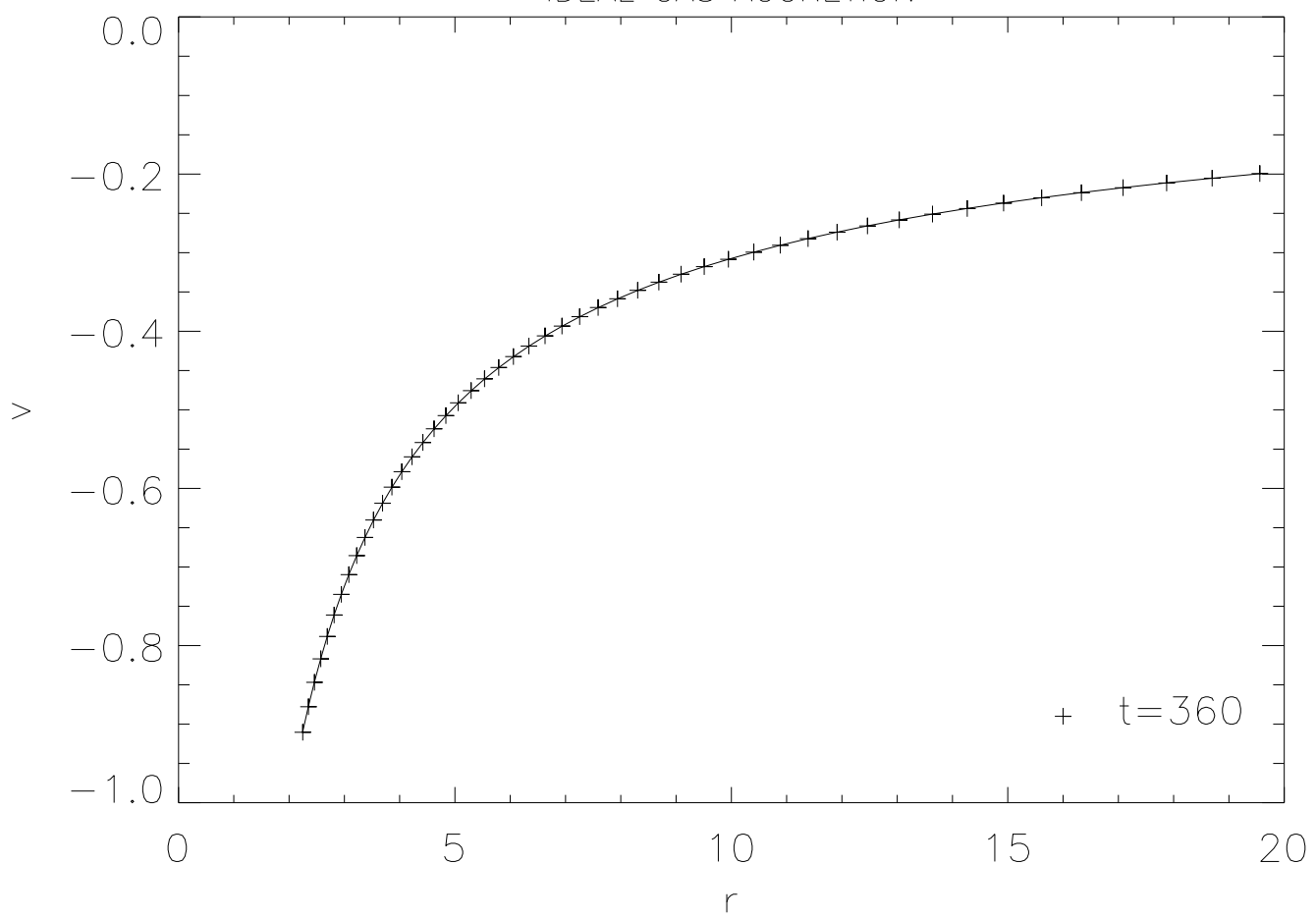
Figure 18b.- Snapshots of the geometrical quantity α^2 as a function of the radial coordinate (model B). Labels stand , respectively, for the following values of time (in msec.): 80.68, 80.93, 81.76 and 86.51

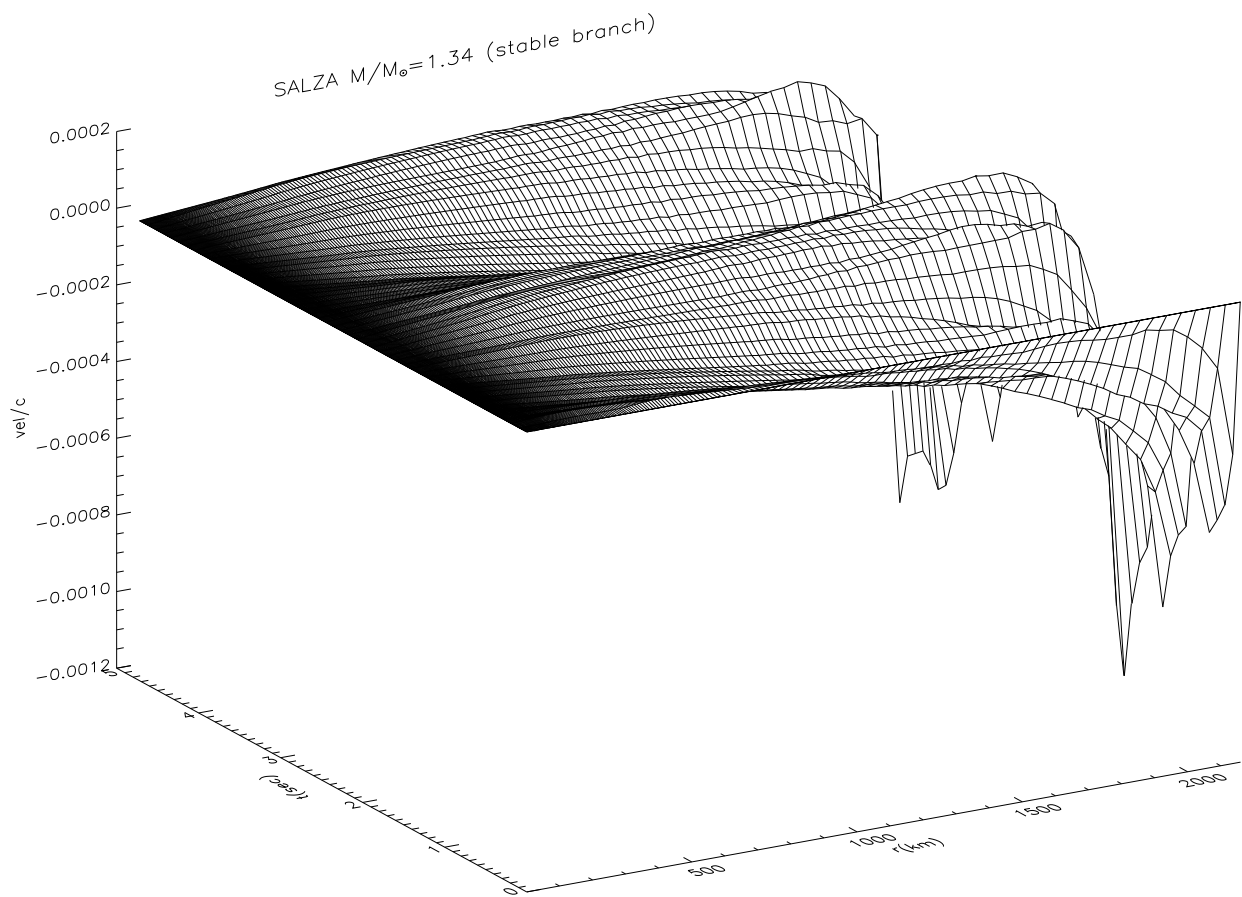
SHOCK REFLECTION TEST (SPHERICAL SYMMETRY) $v=0.99999$

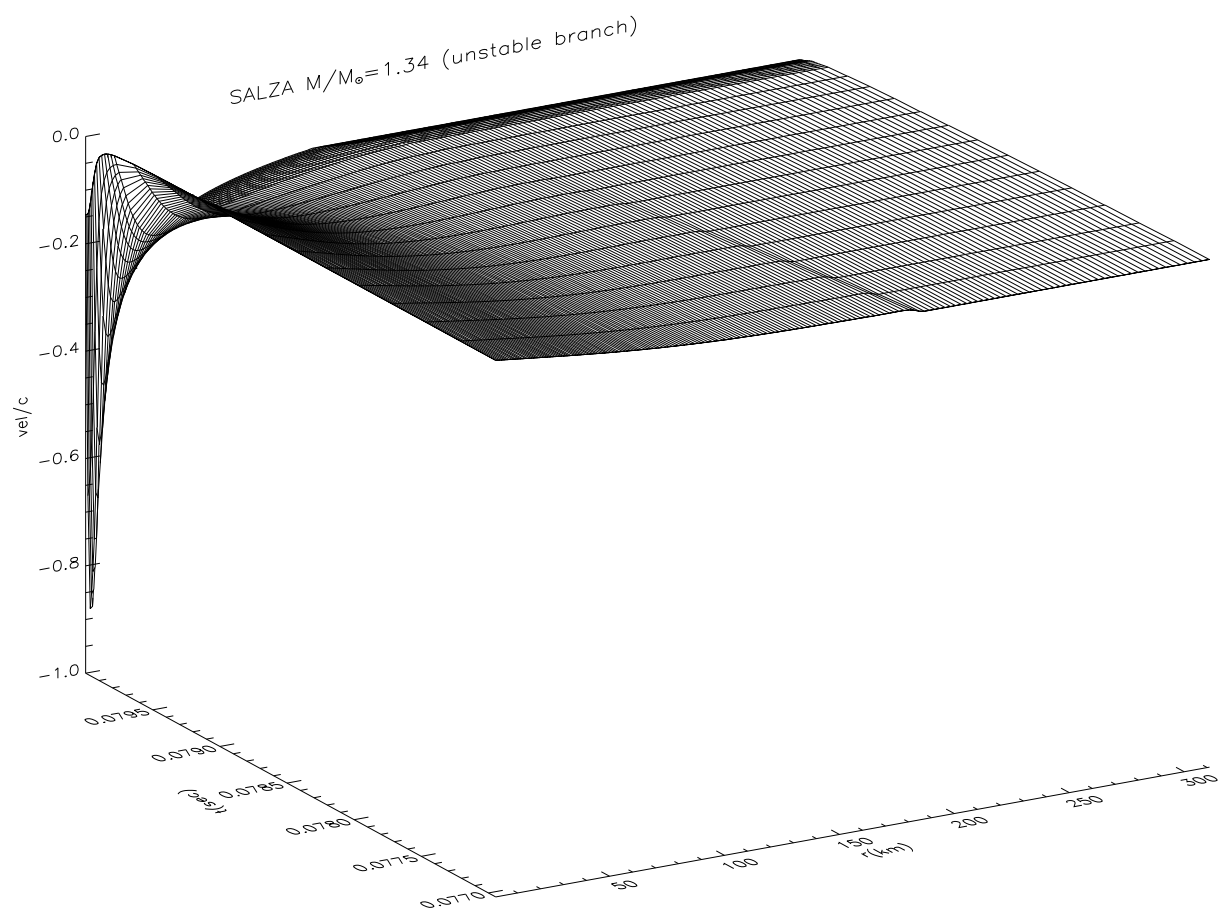


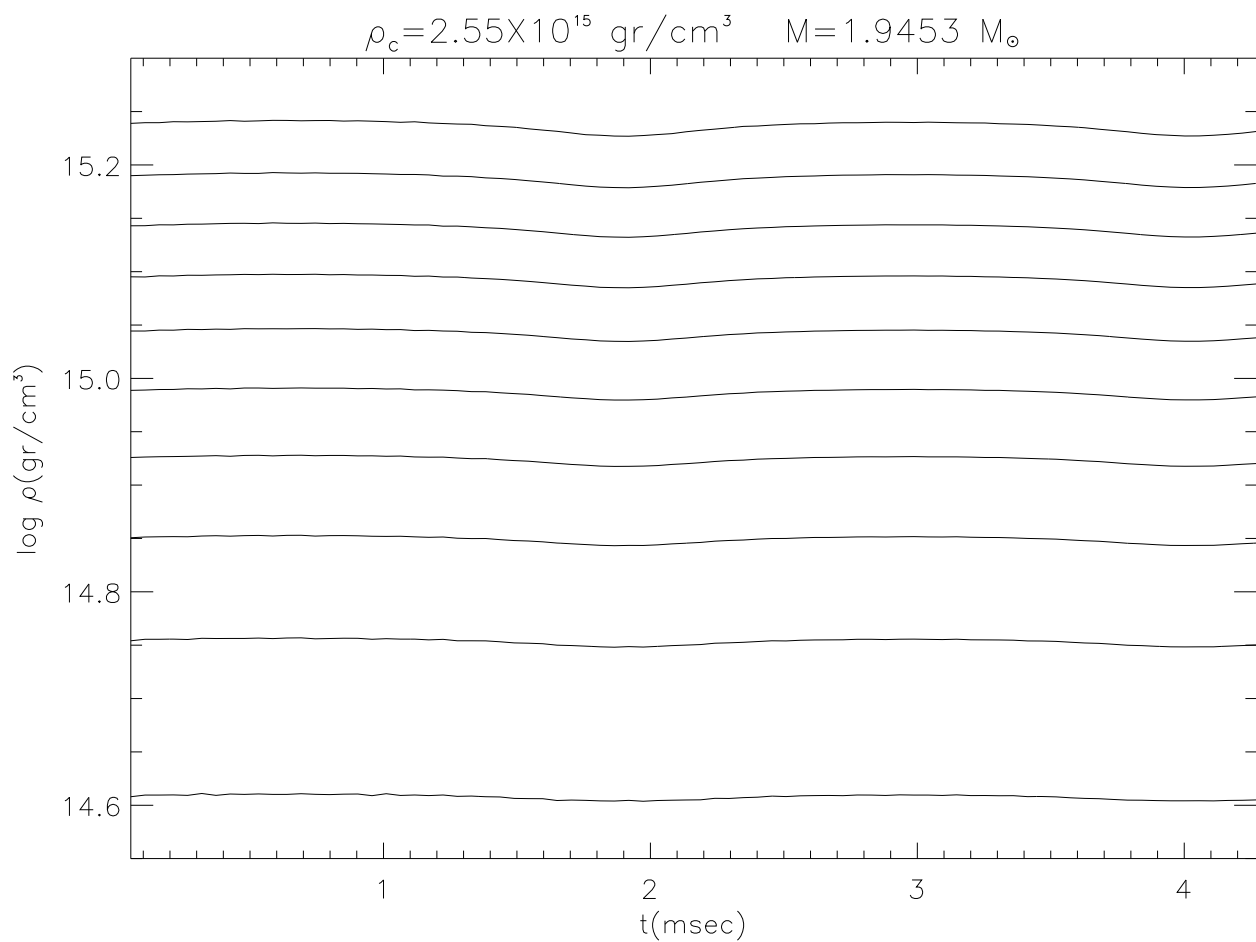


IDEAL GAS ACCRETION









$$\rho_c = 2.57 \times 10^{15} \text{ gr/cm}^3 \quad M = 1.9452 \text{ M}_\odot$$

